Supporting Information

Probing the Structure–Property Relationships of Supported Copper Oxide Nanoclusters for Methane Activation

Xijun Wang, Kaihang Shi, Anyang Peng, and Randall Q. Snurr*

Department of Chemical and Biological Engineering, Northwestern University, Evanston, IL 60208, USA

*Email: snurr@northwestern.edu

Keywords: Copper oxide, nanocluster, methane activation, heterogeneous catalysis, electronic structure, descriptor

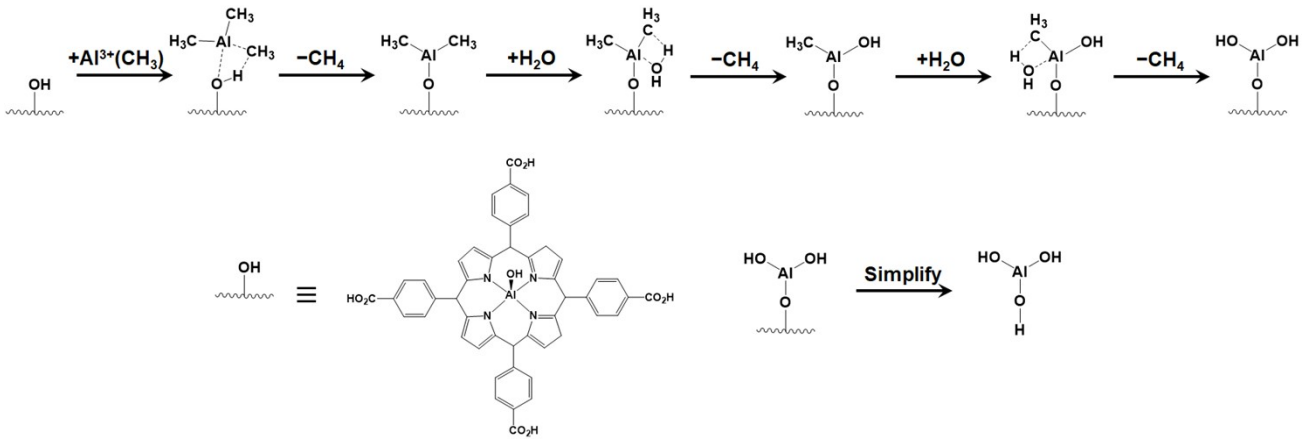

Fig. S1. Proposed mechanism for the aluminum (III) ALD process.

In our previous study,[1] we constructed the support model using aluminum(III) hydroxo tetrakis (4-carboxyphenyl) porphyrin (Al^{III}(OH)-TCPP). This model was derived by cutting the Fe-TCPP linker from the crystal structure of the PCN-222(Fe) MOF[2] and substituting the Fe with the more readily modeled Al. To simplify the support model further, we substituted the Al^{III}-TCPP moiety with a hydrogen atom, given that this simplification has a negligible impact on the energetics associated with methane activation.[1] For instance, the activation barrier of methane on a certain di-copper oxide nanocluster is 59.5 kJ/mol with the Al^{III}(OH)-TCPP support, versus 57.0 kJ/mol when substituting the support with a hydrogen atom. Although the hydrogen atom serves as a model for the substrate in our calculations, fixing a single atom in DFT is essentially the same as allowing full relaxation of all atoms. As such, our approach involves the complete relaxation of all atoms.

Table. S1. Relative free energies at 473 K (in kJ/mol) for the key tetra-copper oxide nanoclusters at relevant spin states. For each nanocluster, the most stable spin state is set as the energy reference. The notation $\langle \hat{S}^2 \rangle$ represents the expectation value of the squared total spin operator for the most stable spin state of each nanocluster.

Spin multiplicity	1	2	3	4	5	6	$\langle \hat{S}^2 \rangle$
Ref	12.82	–	0.00	–	150.27	–	2.0002
I	74.36	–	20.29	–	0.00	–	6.0003
II	75.74	–	18.96	–	0.00	–	6.0003
III	4.19	–	3.63	–	0.00	–	6.0002
IV	81.31	–	0.00	–	5.07	–	2.0238
V	78.05	–	0.00	–	5.28	–	2.0422
VI	10.57	–	3.72	–	0.00	–	6.0002
VII	13.25	–	7.72	–	0.00	–	6.0001
VIII	9.51	–	9.09	–	0.00	–	6.0001
IX	2.28	–	0.00	–	10.89	–	2.0242
I.1	20.94	–	6.02	–	0.00	–	6.0003

I.2	4.55	–	3.82	–	0.00	–	6.0002
I.3	74.56	–	19.23	–	0.00	–	6.0003
I.4	23.22	–	20.70	–	0.00	–	6.0006
I.5	15.72	–	12.74	–	0.00	–	6.0004
I.6	25.11	–	16.98	–	0.00	–	6.0004
I.7	36.40	–	12.84	–	0.00	–	6.0004
I.8	28.57	–	7.96	–	0.00	–	6.0004
I.9	72.01	–	10.78	–	0.00	–	6.0003
I.10	43.47	–	0.00	–	1.23	–	2.0029
I.11	18.00	–	14.01	–	0.00	–	6.0003
I.12	69.90	–	17.50	–	0.00	–	6.0003
I.13	48.66	–	0.00	–	7.21	–	2.0096
I.14	72.14	–	0.61	–	0.00	–	6.0003
I.15	48.78	–	0.00	–	2.69	–	2.0390
I.16	50.59	–	13.33	–	0.00	–	6.0003
I.17	51.14	–	2.03	–	0.00	–	6.0003
I.18	10.43	–	0.00	–	0.98	–	2.0390
I.19	92.70	–	16.88	–	0.00	–	6.0003
I.20	73.87	–	0.15	–	0.00	–	6.0003
I.21	71.96	–	2.39	–	0.00	–	6.0003
I.22	12.07	–	20.02	–	0.00	–	6.0003
I.23	11.09	–	7.09	–	0.00	–	6.0003
I.24	13.01	–	12.80	–	0.00	–	6.0003
I.25	5.21	–	5.17	–	0.00	–	6.0003
I.26	5.24	–	13.38	–	0.00	–	6.0003
I.27	5.46	–	11.93	–	0.00	–	6.0003
I.28	23.98	–	9.42	–	0.00	–	6.0003
I.29	5.46	–	11.88	–	0.00	–	6.0003
I.30	45.77	–	0.00	–	8.97	–	2.0103
I.31	74.90	–	0.00	–	25.53	–	2.0329
I.32	24.78	–	10.92	–	0.00	–	6.0003
I.33	53.58	–	3.07	–	0.00	–	6.0004
I.34	16.92	–	11.96	–	0.00	–	6.0004
I.35	62.43	–	26.71	–	0.00	–	6.0003
I.36	8.64	–	6.03	–	0.00	–	6.0003
I.37	61.17	–	10.96	–	0.00	–	6.0003
I.38	19.27	–	16.78	–	0.00	–	6.0003
I.39	65.63	–	14.51	–	0.00	–	6.0005
I.40	103.57	–	18.29	–	0.00	–	6.0004
I.41	80.21	–	4.34	–	0.00	–	6.0003
I.42	49.19	–	5.69	–	0.00	–	6.0003
I.43	62.11	–	18.81	–	0.00	–	6.0003
I.44	44.75	–	0.00	–	6.13	–	2.0095
I.45	50.53	–	6.53	–	0.00	–	6.0003
I.46	88.93	–	30.09	–	0.00	–	6.0004
I.47	71.41	–	36.40	–	0.00	–	6.0004
I.48	61.70	–	0.00	–	12.72	–	2.0176
I.49	55.46	–	6.10	–	0.00	–	6.0003
I.50	77.17	–	25.23	–	0.00	–	6.0004
I.51	75.83	–	0.00	–	19.45	–	2.0197
I.52	75.12	–	0.00	–	18.19	–	2.0196
I.53	88.58	–	18.87	–	0.00	–	6.0004
I.54	75.13	–	0.00	–	26.77	–	2.0198
I.55	73.21	–	23.56	–	0.00	–	6.0004
I.56	59.65	–	18.80	–	0.00	–	6.0004
I.57	88.13	–	12.24	–	0.00	–	6.0004
I.58	90.35	–	10.97	–	0.00	–	6.0006
I.59	88.48	–	11.64	–	0.00	–	6.0006
I.60	75.91	–	0.00	–	19.37	–	2.0198
I.61	87.96	–	12.80	–	0.00	–	6.0004

I.62	85.60	–	12.24	–	0.00	–	6.0004
I.63	88.23	–	12.75	–	0.00	–	6.0004
I.64	78.66	–	0.22	–	0.00	–	6.0005
V.1	82.54	–	6.81	–	0.00	–	6.0002
V.2	29.87	–	0.00	–	40.14	–	2.0003
V.3	36.99	–	0.00	–	43.06	–	2.0003
V.4	31.72	–	0.00	–	47.68	–	2.0003
V.5	46.72	–	0.00	–	49.70	–	2.0002
V.6	36.62	–	0.00	–	11.49	–	2.0029
V.7	37.61	–	0.00	–	17.81	–	2.0079
V.8	39.47	–	0.00	–	45.55	–	2.0169
V.9	16.32	–	0.00	–	6.35	–	2.0039
V.10	21.75	–	0.00	–	Unstable	–	2.0001
V.11	0.00	–	19.34	–	54.11	–	0.0000
V.12	10.26	–	43.00	–	0.00	–	6.0001
V.13	49.08	–	11.62	–	0.00	–	6.0001
V.14	37.64	–	95.70	–	0.00	–	6.0001
V.15	5.72	–	0.00	–	Unstable	–	2.0001
V.16	1.47	–	0.22	–	0.00	–	6.0001
V.17	15.60	–	2.02	–	0.00	–	6.0001
V.18	0.00	–	2.48	–	Unstable	–	2.0058
V.19	25.19	–	0.00	–	6.40	–	2.0073

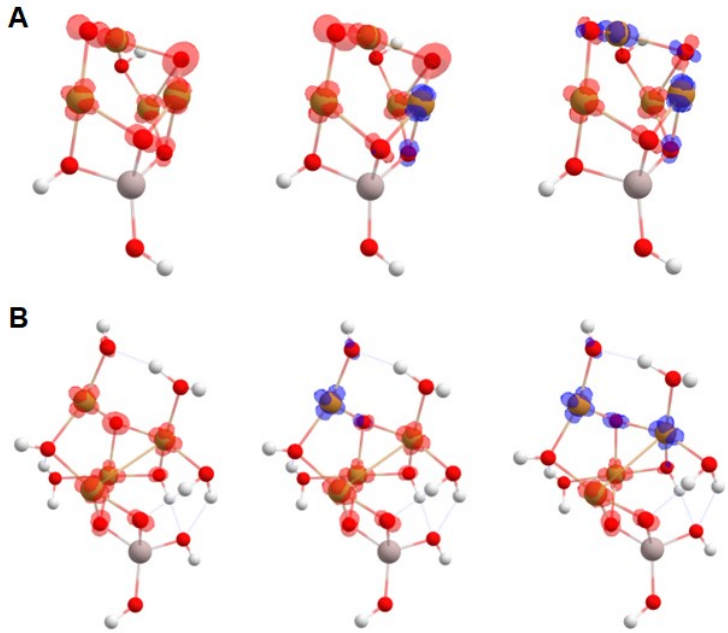

Fig. S2. Possible spin density distribution of configurations (A) I.9 and (B) V.1. The structures from left to right represent the high spin (ferromagnetic) state, followed by the ferrimagnetic and antiferromagnetic broken spin states. Red and blue bubbles denote unpaired spin-up and spin-down electrons, respectively. Refer to **Table S2** for the corresponding exchange coupling constants.

Table S2. Computed parameters and exchange coupling constants associated with the broken symmetry for possible spin states of I.9 and V.1. Refer to **Fig. S2** for the corresponding spin density visualizations.

System	High-spin (HS) $\langle S^2 \rangle$	Broken symmetry (BS) $\langle S^2 \rangle$	S_{max}	$E_{HS} - E_{BS}$ (eV)	Exchange coupling Constant (J) (cm^{-1})*
I.9 Ferrimagnetic	6.03	2.94	2	–0.10	204.34
I.9 Antiferromagnetic	6.03	1.89	2	–0.27	551.06
V.1 Ferrimagnetic	6.02	2.92	2	–0.05	101.97
V.1 Antiferromagnetic	6.02	1.93	2	–0.05	107.89

*Computed with ORCA package[3] using the formula $J = -(E_{HS} - E_{BS})/S_{max}^2$.[4-6]

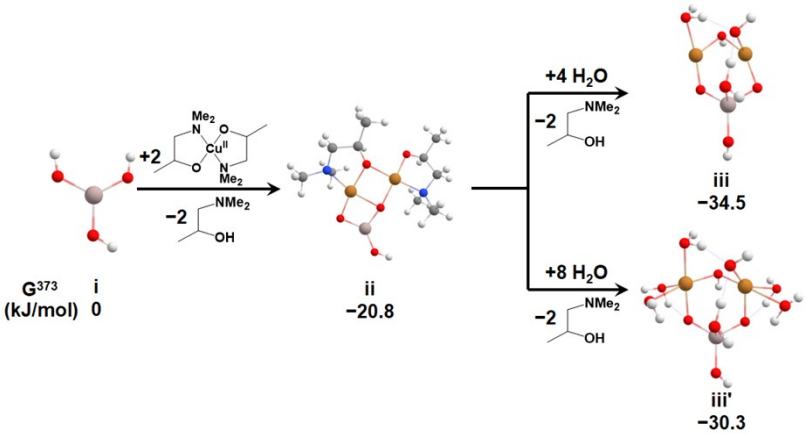

Fig. S3. Comparison of the Gibbs free energies for iii ($Cu_2AlO_7H_7$) and iii' ($Cu_2AlO_{11}H_{15}$) in the proposed ALD scheme at $P_{Cu(dmap)_2}$= P_{H_2O}= 1 Torr, P_{Hdmap} = 10^{-7} Torr, and T =373 K. Dark grey, blue, white, red, golden, and light peach spheres represent C, N, H, O, Cu, and Al atoms, respectively.

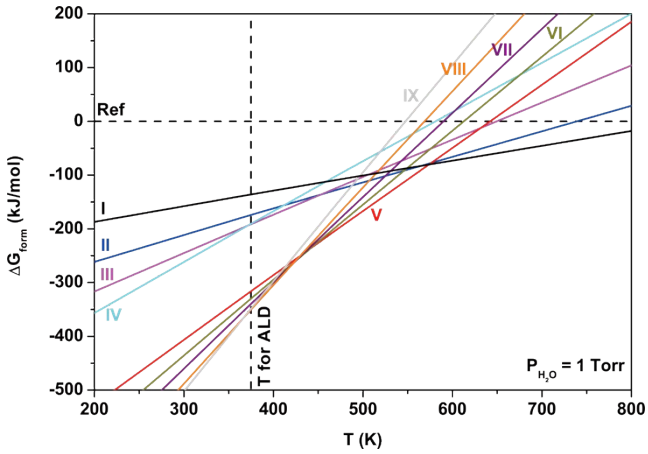

Fig. S4. Phase diagram of various Cu_4O-NCs at the experimental P_{H_2O} (1 Torr). Corresponding

structures are shown in **Fig. 2**.

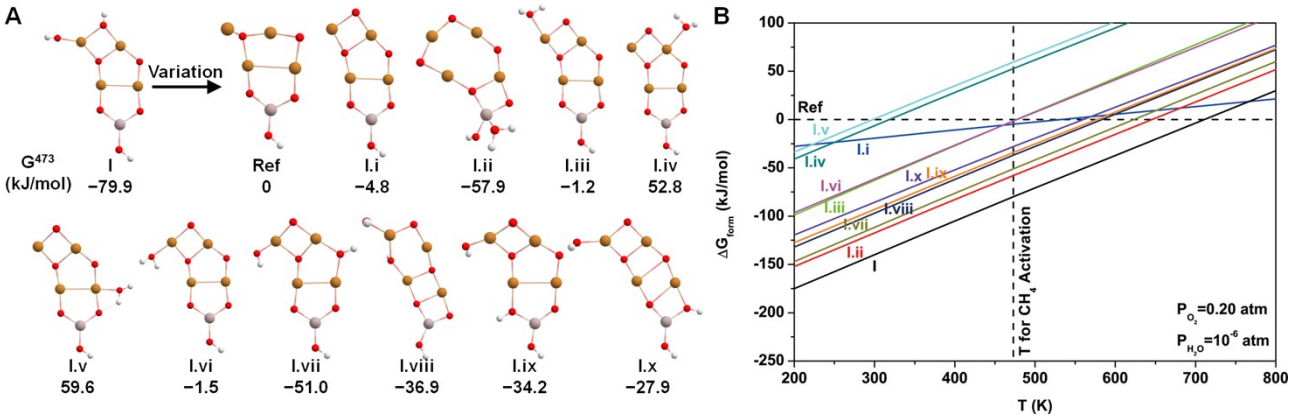

Fig. S5. (A) Optimized geometric structures and (B) corresponding phase diagram of configuration I and its variants. White, red, golden, and light peach spheres represent H, O, Cu, and Al atoms, respectively. The phase diagram was drawn at the experimental partial pressure of methane activation (P_{O_2}= 0.2 atm, P_{H_2O}= 10^{-6} atm).

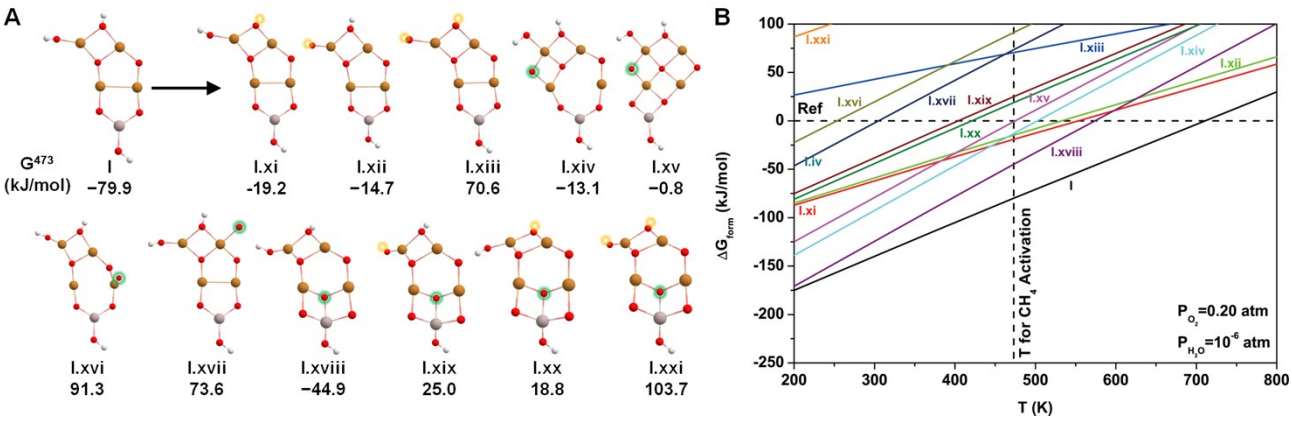

Fig. S6. (A) Optimized geometric structures and (B) corresponding phase diagram of configuration I and its variants obtained after oxidative dehydrogenation and/or oxidation on various sites of I. White, red, golden, and light peach spheres represent H, O, Cu, and Al atoms, respectively. Yellow and green bubbles denote hydrogen vacancy and additional oxygen atoms, respectively. The phase diagram was drawn at the experimental partial pressure of methane activation (P_{O_2}= 0.2 atm, P_{H_2O}= 10^{-6} atm).

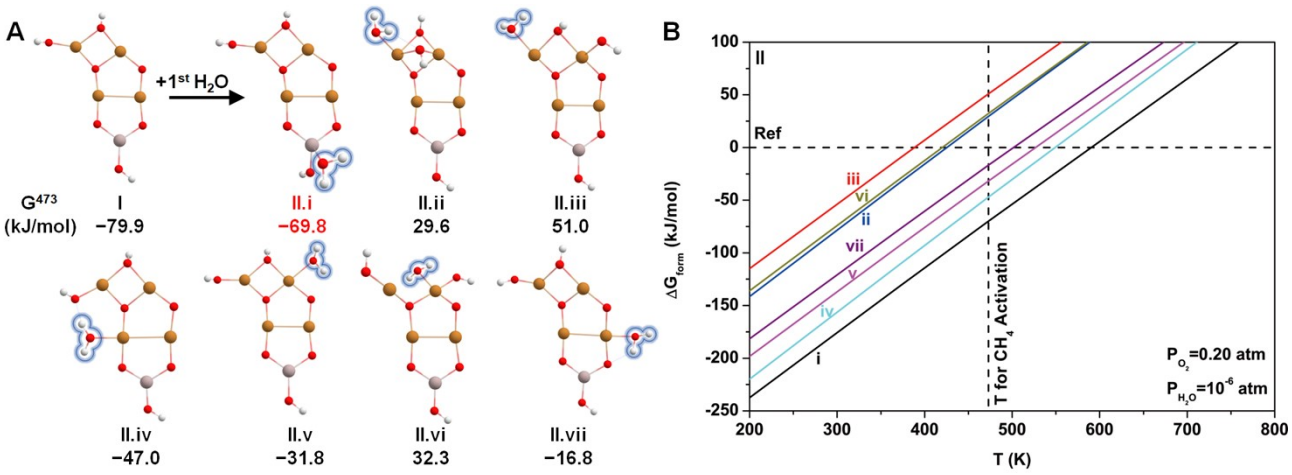

Fig. S7. (A) Optimized geometric structures and (B) corresponding phase diagram of the variants obtained by adding a H_2O (bubbles highlighted) on various sites of configuration I. White, red, golden, and light peach spheres represent H, O, Cu, and Al atoms, respectively. The phase diagram was drawn at the experimental partial pressure of methane activation (P_{O_2}= 0.2 atm, P_{H_2O}= 10^{-6} atm). Configuration II.i is the most stable among these variants at the studied temperature range and thereby simplified as II.

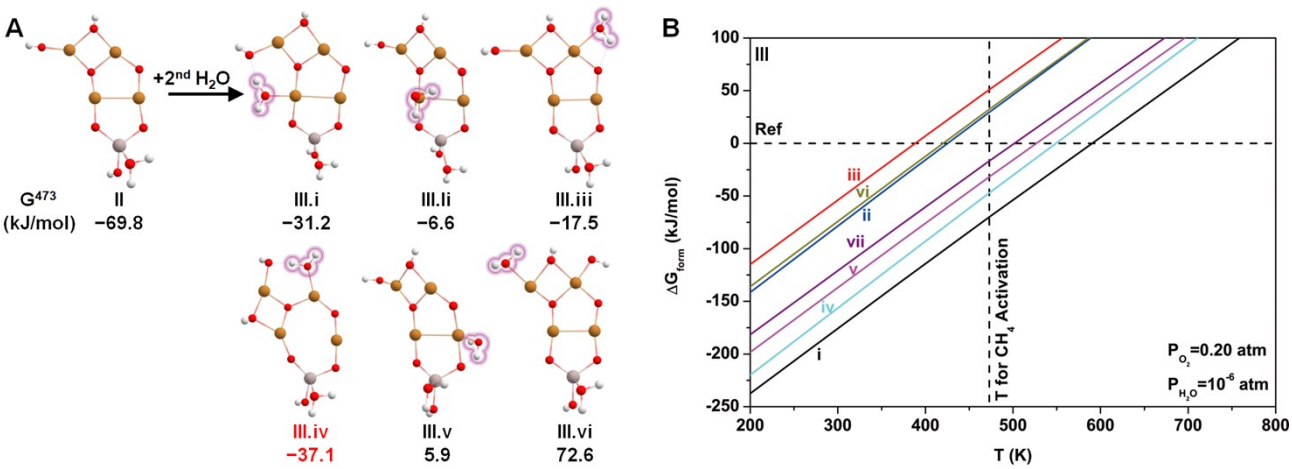

Fig. S8. (A) Optimized geometric structures and (B) corresponding phase diagram of the variants obtained by adding a H_2O (bubbles highlighted) on various sites of configuration II. White, red, golden, and light peach spheres represent H, O, Cu, and Al atoms, respectively. The phase diagram was drawn at the experimental partial pressure of methane activation (P_{O_2}= 0.2 atm, P_{H_2O}= 10^{-6} atm). Configuration III.iv is the most stable among these variants at the studied temperature range and thereby simplified as III.

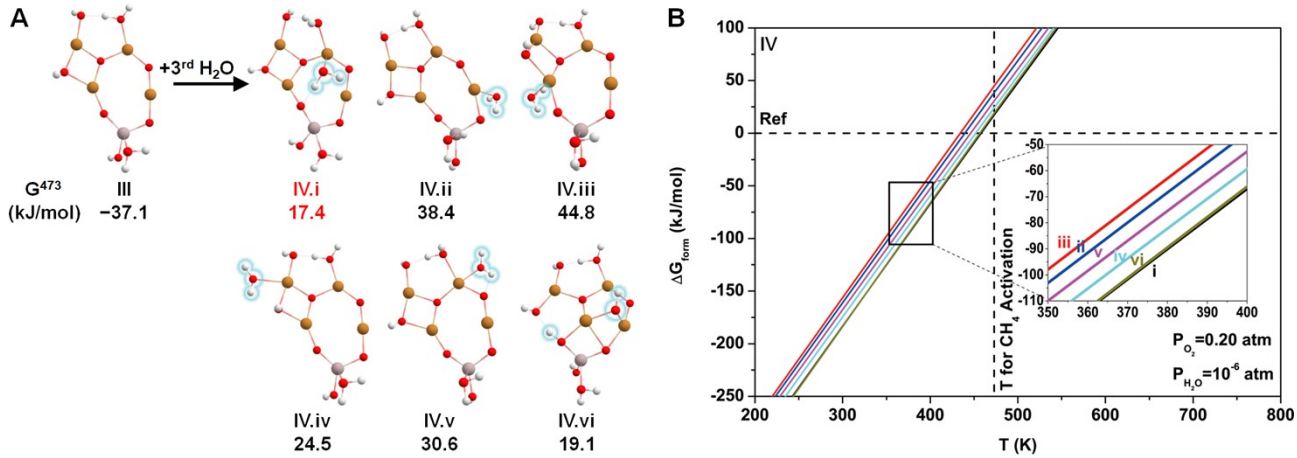

Fig. S9. (A) Optimized geometric structures and (B) corresponding phase diagram of the variants obtained by adding a H_2O (bubbles highlighted) on various sites of configuration III. White, red, golden, and light peach spheres represent H, O, Cu, and Al atoms, respectively. The phase diagram was drawn at the experimental partial pressure of methane activation (P_{O_2}= 0.2 atm, P_{H_2O}= 10^{-6} atm). Configuration IV.i is the most stable among these variants at the studied temperature range and thereby simplified as IV.

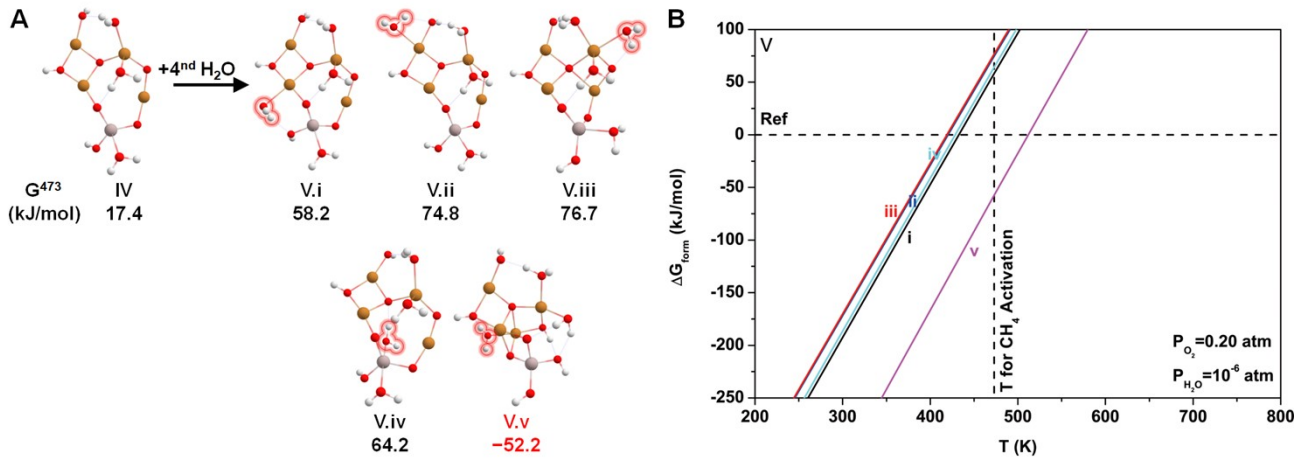

Fig. S10. (A) Optimized geometric structures and (B) corresponding phase diagram of the variants obtained by adding a H_2O (bubbles highlighted) on various sites of configuration IV. White, red, golden, and light peach spheres represent H, O, Cu, and Al atoms, respectively. The phase diagram was drawn at the experimental partial pressure of methane activation (P_{O_2}= 0.2 atm, P_{H_2O}= 10^{-6} atm). Configuration V.v is the most stable among these variants at the studied temperature range and

thereby simplified as V.

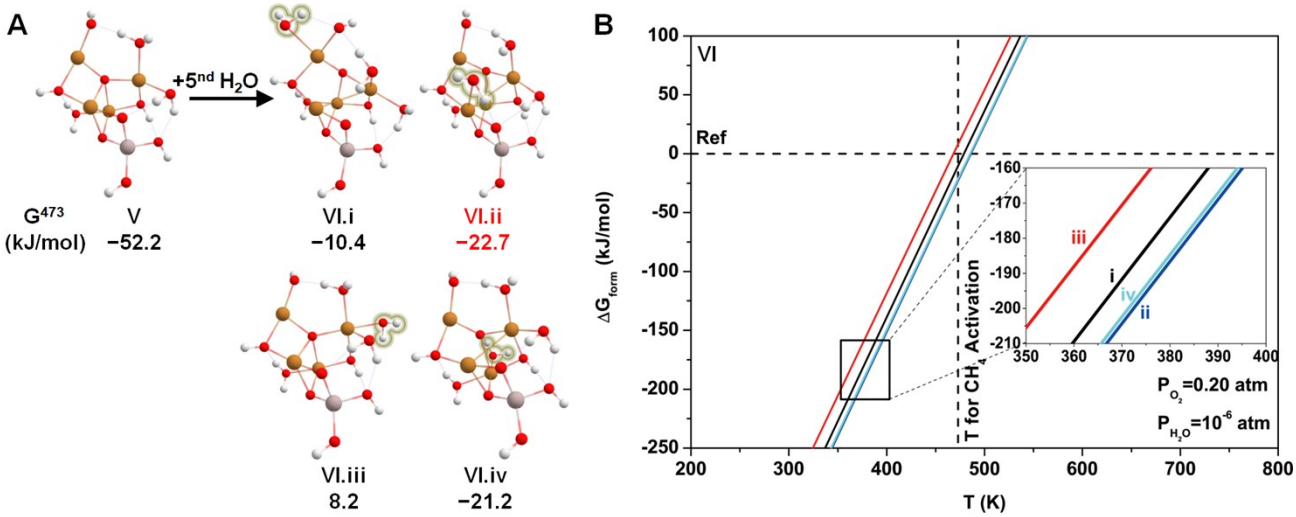

Fig. S11. (A) Optimized geometric structures and (B) corresponding phase diagram of the variants obtained by adding a H_2O (bubbles highlighted) on various sites of configuration V. White, red, golden, and light peach spheres represent H, O, Cu, and Al atoms, respectively. The phase diagram was drawn at the experimental partial pressure of methane activation (P_{O_2}= 0.2 atm, P_{H_2O}= 10^{-6} atm). Configuration VI.ii is the most stable among these variants at the studied temperature range and thereby simplified as VI.

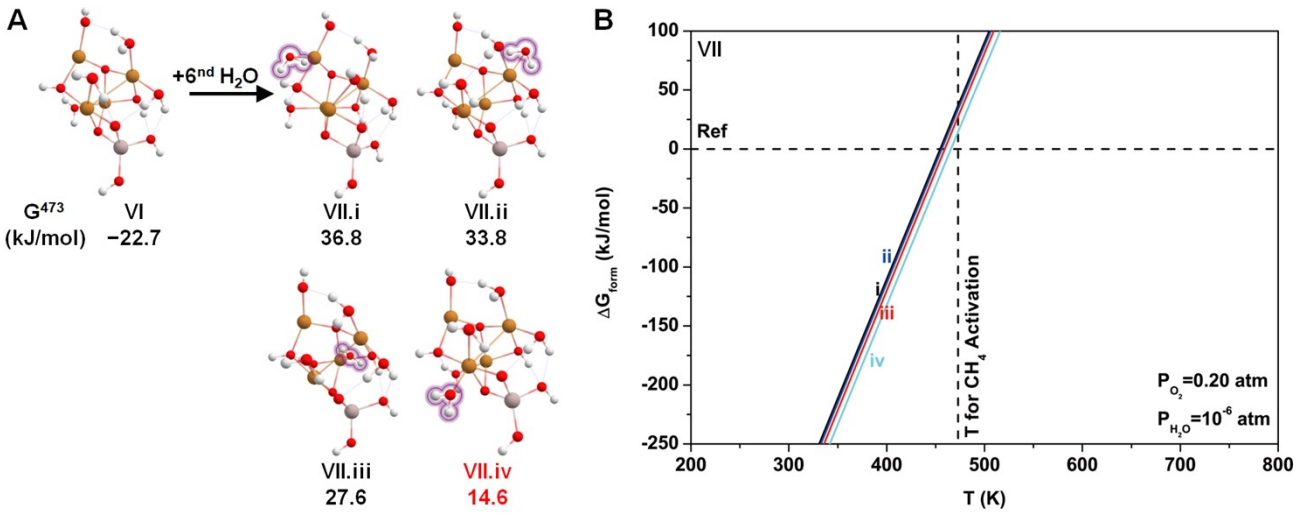

Fig. S12. (A) Optimized geometric structures and (B) corresponding phase diagram of the variants obtained by adding a H_2O (bubbles highlighted) on various sites of configuration VI. White, red, golden, and light peach spheres represent H, O, Cu, and Al atoms, respectively. The phase diagram was drawn at the experimental partial pressure of methane activation (P_{O_2}= 0.2 atm, P_{H_2O}= 10^{-6}

atm). Configuration VII.iv is the most stable among these variants at the studied temperature range and thereby simplified as VII.

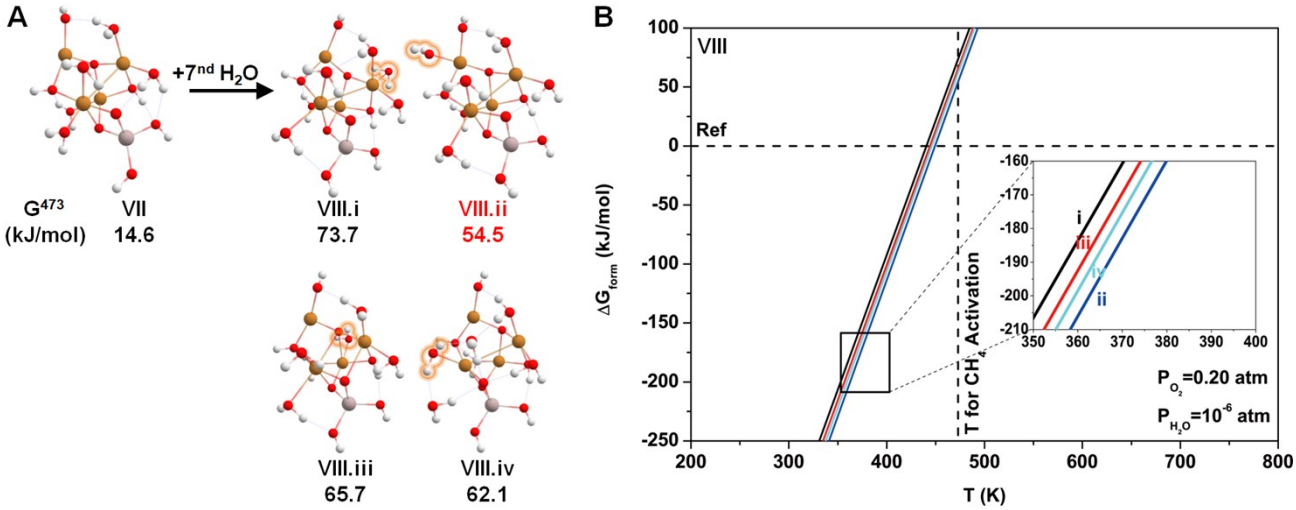

Fig. S13. (A) Optimized geometric structures and (B) corresponding phase diagram of the variants obtained by adding a H_2O (bubbles highlighted) on various sites of configuration VII. White, red, golden, and light peach spheres represent H, O, Cu, and Al atoms, respectively. The phase diagram was drawn at the experimental partial pressure of methane activation (P_{O_2}= 0.2 atm, P_{H_2O}= 10^{-6} atm). Configuration VIII.ii is the most stable among these variants at the studied temperature range and thereby simplified as VIII.

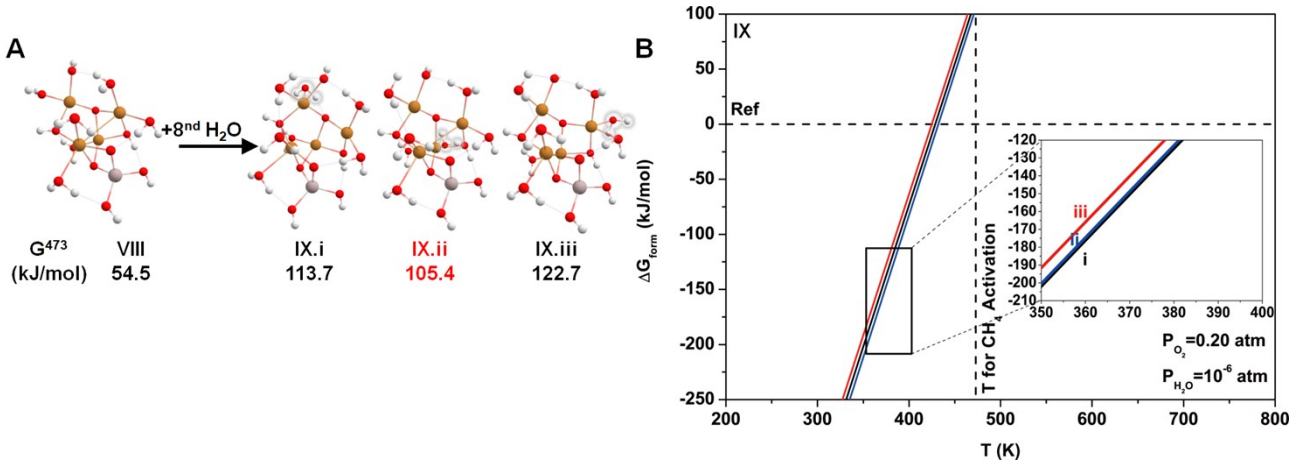

Fig. S14. (A) Optimized geometric structures and (B) corresponding phase diagram of the variants obtained by adding a H_2O (bubbles highlighted) on various sites of configuration VIII. White, red, golden, and light peach spheres represent H, O, Cu, and Al atoms, respectively. The phase diagram

was drawn at the experimental partial pressure of methane activation (P_{O_2}= 0.2 atm, P_{H_2O}= 10^{-6} atm). Configuration IX.ii is the most stable among these variants at the studied temperature range and thereby simplified as IX.

Table. S3. Evolution of key bond lengths (Å) around the active oxygen sites over time in AIMD simulations for configurations I.9, I.19, I.53, V.1, V.4, and V.6.

	Bond	0 fs	50 fs	100 fs	150 fs	200 fs
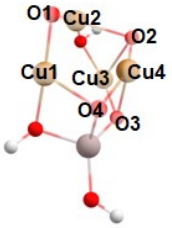	O1-Cu1	1.815	1.778	1.747	1.788	1.771
	O1-Cu2	1.823	1.811	1.802	1.742	1.766
	O2-Cu2	2.008	1.993	1.986	1.982	1.980
	O2-Cu3	1.851	2.020	1.995	1.972	1.951
	O2-Cu4	2.049	1.977	2.079	2.141	2.159
	O3-Cu3	1.860	1.845	1.828	1.811	1.801
	O3-Cu4	2.095	2.070	2.050	2.041	2.044
	O4-Cu1	2.051	2.050	2.057	2.074	2.103
I.9	O4-Cu4	1.862	1.778	1.716	1.701	1.739
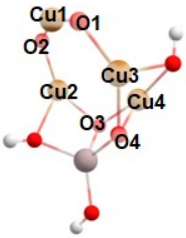	O1-Cu1	1.783	1.758	1.742	1.741	1.756
	O1-Cu3	1.796	1.790	1.782	1.773	1.764
	O2-Cu1	1.776	1.813	1.843	1.854	1.842
	O2-Cu2	1.793	1.858	1.909	1.933	1.925
	O3-Cu2	1.971	1.949	1.931	1.921	1.920
	O3-Cu4	1.858	1.848	1.844	1.849	1.860
	O4-Cu3	1.905	1.866	1.837	1.828	1.838
I.19	O4-Cu4	2.031	2.003	1.976	1.953	1.934
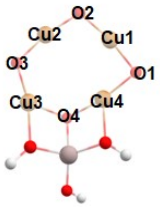	O1-Cu1	1.778	1.768	1.762	1.765	1.775
	O1-Cu4	1.810	1.830	1.843	1.845	1.834
	O2-Cu1	1.765	1.828	1.872	1.885	1.865
	O2-Cu2	1.762	1.730	1.710	1.710	1.728
	O3-Cu2	1.753	1.727	1.712	1.714	1.729
	O3-Cu3	1.777	1.812	1.834	1.832	1.807
	O4-Cu3	1.961	1.984	2.012	2.047	2.086
I.53	O4-Cu4	1.899	1.915	1.928	1.934	1.930
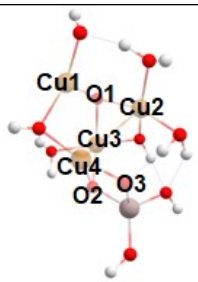	O1-Cu1	1.901	1.908	1.916	1.922	1.920
	O1-Cu2	1.964	2.026	2.080	2.118	2.136
	O1-Cu3	1.991	2.014	2.037	2.056	2.070
	O2-Cu3	1.984	1.979	1.978	1.980	1.985
	O2-Cu4	2.039	2.075	2.110	2.138	2.158
	O3-Cu4	1.816	1.776	1.749	1.744	1.761
V.1						
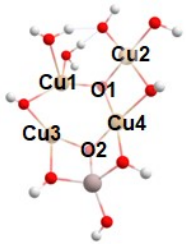	O1-Cu1	1.886	1.863	1.836	1.812	1.796
	O1-Cu2	1.850	1.868	1.893	1.912	1.922
	O1-Cu4	1.943	1.992	2.027	2.044	2.041
	O2-Cu3	1.896	1.902	1.911	1.925	1.942
	O2-Cu4	1.938	1.973	2.003	2.023	2.028
V.4						
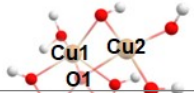	O1-Cu1	1.990	1.869	1.798	1.762	1.773
	O1-Cu2	1.941	1.896	1.888	1.882	1.880
	O1-Cu3	2.235	2.160	2.186	2.205	2.213

	O1-Cu4	2.032	2.301	2.325	2.324	2.291
	O2-Cu3	1.833	1.797	1.798	1.815	1.835
	O2-Cu4	1.945	1.986	2.000	2.005	1.994

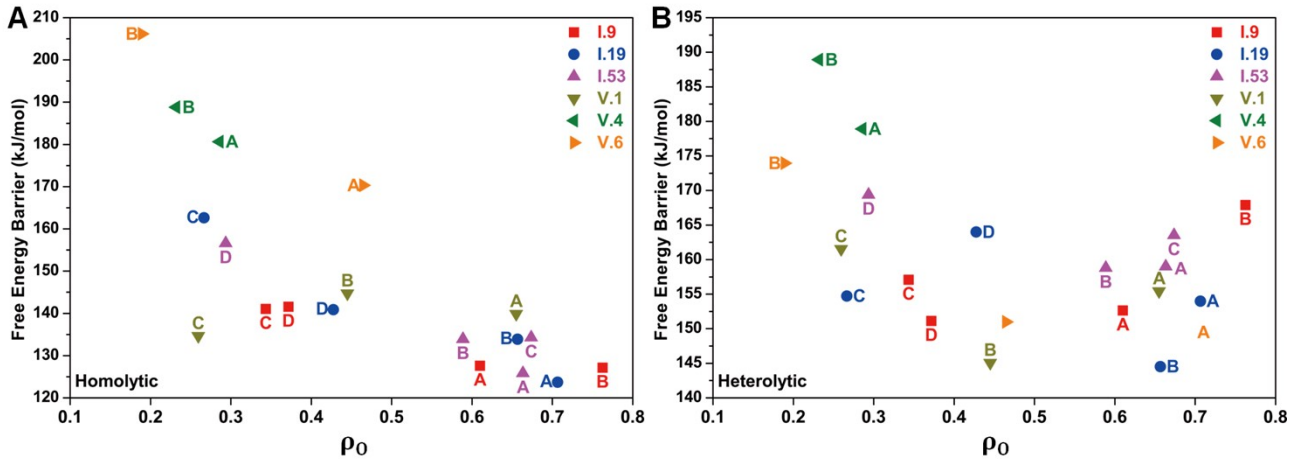

Fig. S15. Correlations between the spin density on the oxygen atom (ρ_O) and the DFT-computed (A) $\Delta G_{homo}^{\ddagger}$ and (B) $\Delta G_{heter}^{\ddagger}$ for methane activation at each oxygen site on I.9, I.19, I.53, V.1, V.4, and V.6.

DFT optimized key structure coordinates are provided in separate files as follows:

1. **Figure 1**:
    - Files: **i.xyz**, **ii.xyz**, **iii.xyz**, **iv.xyz**
    - Location: **Str-1/Str-Fig1**
2. **Figure 2**:
    - Files: **Ref.xyz**, **I.xyz**, **II.xyz**, **III.xyz**, **IV.xyz**, **V.xyz**, **VI.xyz**, **VII.xyz**, **VIII.xyz**, **IX.xyz**
    - Location: **Str-1/Str-Fig2**
3. **Figure 3**:
    - Files: **I.1.xyz** to **I.64.xyz**
    - Location: **Str-2/Str-Fig3-part1**, **Str-3/Str-Fig3-part2**
4. **Figure 5**:
    - Files:
        - **I.9-homolytic-A.xyz** to **I.9-homolytic-D.xyz**
        - **I.9-heterolytic-A.xyz** to **I.9-heterolytic-D.xyz**
        - **I.19-homolytic-A.xyz** to **I.19-homolytic-D.xyz**
        - **I.19-heterolytic-A.xyz** to **I.19-heterolytic-D.xyz**
        - **I.53-homolytic-A.xyz** to **I.53-homolytic-D.xyz**
        - **I.53-heterolytic-A.xyz** to **I.53-heterolytic-D.xyz**
    - Location: **Str-4/Str-Fig5**
5. **Figure 6**:
    - Files: **V.1.xyz** to **V.19.xyz**
    - Location: **Str-5/Str-Fig6**
6. **Figure 7**:
    - Files:
        - **V.1-homolytic-A.xyz** to **V.1-homolytic-C.xyz**
        - **V.1-heterolytic-A.xyz** to **V.1-heterolytic-C.xyz**
        - **V.4-homolytic-A.xyz** to **V.4-homolytic-C.xyz**
        - **V.4-heterolytic-A.xyz** to **V.4-heterolytic-C.xyz**
        - **V.6-homolytic-A.xyz** to **V.6-homolytic-C.xyz**
        - **V.6-heterolytic-A.xyz** to **V.6-heterolytic-C.xyz**
    - Location: **Str-5/Str-Fig7**

References

1. H. A. Doan, Z. Li, O. K. Farha, J. T. Hupp and R. Q. Snurr, *Catal. Today*, 2018, **312**, 2–9.
2. D. Feng, Z.-Y. Gu, J.-R. Li, H.-L. Jiang, Z. Wei and H.-C. Zhou, *Angew. Chem.*, 2012, **124**, 10453–10456.
3. F. Neese, *Wiley Interdiscip. Rev. Comput. Mol. Sci.*, 2012, **2** (1), 73–78.
4. A.P. Ginsberg, *J. Am. Chem. Soc.*, 1980, **102**, 111.
5. L. Noodleman, *J. Chem. Phys.*, 1981, **74**, 5737.
6. L. Noodleman and E.R. Davidson, *Chem. Phys.*, 1986, **109**, 131.